Time-dependent spatial distribution of thermal stresses in the ice cover of a small reservoir

Chris Petrich[1*], Irina Sæther[1], Lennart Fransson[2], Bjørnar Sand[1], and Bård Arntsen[1]

[1]: Northern Research Institute (Norut) Narvik, Narvik, Norway

[2]: Luleå University of Technology, Luleå, Sweden

[*]: corresponding author email: christian.petrich@norut.no

Abstract

Static ice loads (ice actions) are a key design parameter for dams in cold climates. However, their theoretical description is still elusive, introducing uncertainty in design and hindering development of remediation measures. We present and analyze measurements of stresses due to thermal loads in a small reservoir in northern Norway. Several weeks of observations, including both cold and warm spells, were well-described by a simple equation that accounts for thermal expansion and temperature-dependent creep. One model parameter was found to depend systematically on the location of measurements within the reservoir. Biaxial stress measurements showed that the stress field was not homogeneous. Results suggest that the stress field in reservoirs should be predictable from first principles with numerical methods and point toward a promising, simple parameterization.

1 Introduction

Design rules and practices have been established in several countries to ensure the safety of hydropower dams. One design parameter is static ice load, resulting from thermal expansion of the ice cover or water level fluctuations (e.g. Comfort et al., 2003). Ice loads are variable actions whose intensity and/or points of application vary frequently and significantly over time (CFBR, 2013). Design standards are based on limited empirical measurements as current understanding of the magnitude of ice loads is still limited (Timco et al., 1996; Comfort et al., 2003; Gebre et al., 2013). Since field measurements of ice forces on dams have suggested that maximum static ice loads depend significantly on the location of the dam, climate and sudden temperature changes, increasing efforts to understand ice loads on dams has been called for (Gebre et al., 2013). Benefits could be two-fold: on the one hand, costs may be reduced during dam construction or maintenance. On the other hand, solutions for ice load reductions may be developed: a more profound understanding of the mechanisms involved in ice–structure interactions may lead to the development of more cost efficient strategies for reducing the actual ice-load on dams. This may be of particular interest for the design of dams for small-scale hydropower plants. The potential for cost reductions during the lifetime of dams is exemplified by a recent change in the Norwegian regulation to the Water Resources Act (Vannressursloven) with respect to safety at hydropower plants, implemented in 2010 (Ministry of Petroleum and Energy, 2009). The guidelines and design recommendations include new considerations regarding ice loads on dams (NVE, 2003), that cause a need for upgrading and strengthening of existing dams and infrastructure.

According to the Norwegian guidelines (NVE, 2003), thermal ice loads are assumed to be line loads between 100 and 150 kN/m near the top of the dam. However, during the most recent decades this has been verified in only one measurement campaign during a single season at Silvann dam in the Northern part of Norway (Hoseth and Fransson, 1999).

43   This study focuses on thermal ice loads. Measurements were performed in a reservoir at a time of

44   year when the ice level was kept steady by the balance of a small influx of water from a creek and

45   outflow over the spillway beneath the ice over.

46 2 Methods

47 *2.1 Installation*

48   A weather station and stress cells were installed at Taraldsvikfossen Reservoir near Narvik, 68.4405°

49   N, 17.471° E, 212 m above sea level in December 2012. The reservoir is small (1000 m^3), bound at the

50   western side by a straight concrete gravity dam and extending approximately 30 m in North–South

51   direction (Figure 1). A concrete maintenance hut is situated half way along the dam. Water depth in

52   the reservoir is approximately 6 m at the dam, reducing to 1 m at the eastern shore. The Taraldsvik

53   creek enters the reservoir from the North–East. A weather station was mounted at the maintenance

54   hut, and a 3 m long vertical string of temperature sensors was frozen into the ice to measure the

55   temperature profile through water, ice, snow, and air.

56   As summarized by Cox and Johnson (1983), sensors used for ice stress measurements fall into two

57   categories: cylindrical sensors having an effective modulus much greater than ice, and thin, wide

58   sensors (flat-jacks), preferably having an effective modulus close to that of ice. Flat-jacks and

59   cylindrical stress gauges were found to compare well during a recent series of field measurements in

60   ice-covered reservoirs in Canada (Taras et al., 2011; Morse et al., 2011). In this study, stresses in the

61   ice were monitored with 15 custom designed oil-filled GeoKon 4850 stress cells (essentially the same

62   as those used by Carter et al. (1998) and Taras et al. (2011)). The cells consisted of two rectangular

63   steel plates (100 mm x 200 mm) welded together around the periphery with de-aired oil occupying

64   the space between the plates. A short tube connected the cell to a vibrating wire pressure transducer

65   that also measured temperature with a temperature-dependent resistor. The cells were calibrated by

66   the manufacturer to an accuracy <0.5 kPa. Stress cells were mounted on steel tape at desired vertical

67 separations and attached to wooden support (Figure 2). In each case the center of the upper-most

68 stress cell was 0.2 m below the ice surface at deployment. Two stations along the dam had three

69 stress cells spaced 0.15 m (Stations 3 and 5) while the station toward the center of the reservoir

70 measuring stress normal to the dam (Station W) had cells spaced 0.25 m. All instruments were

71 connected to a CR1000 data logger recording stress data every 5 minutes. A timelapse camera

72 overlooked the NW corner of the dam, including part of the spillway. The camera recorded images at

73 an interval of approximately 30 minutes. A wooden snow depth stake marked in 10 cm intervals was

74 frozen into the ice in view of the camera. Snow depth, freeboard, and ice thickness were measured

75 at 1 cm resolution during site visits throughout the measurement season. Stress cells were deployed

76 on 12 February 2013 (Figure 2). Slots were cut with a chain saw, instruments were deployed attached

77 to wooden support, and the slots were filled with water pumped from the reservoir. With the

78 exception of Stations N and S, all pressure cells were mounted to register stresses in direction normal

79 to the dam. Stations 1 to 6 were placed approximately 1 m in front of the dam into the ice with

80 Stations 1 and 6 located on the flanks rather than the main section of the dam (Figure 1, Table 1).

81 Stations N, S, and W were installed approximately 10 m in front of the dam and rotated 120° with

82 respect to each other in an equilateral triangle with 2 m side length to allow principal stresses to be

83 calculated easily (Holister, 1967).

2.2 Stress data processing

85 By convention, the zero-point of each stress cell was the respective reading of the pressure sensor

86 after immersion into water. Changes of atmospheric pressure were not accounted for in data

87 processing (order of 1 kPa). The following sign convention is used: stresses are positive in

88 compression. In a confined isothermal plate, compressive stresses arise during temperature increase.

89 Principal stresses were calculated for the triangular configuration of stations N, S, and W following

90 Holister (1967). The angle of the first principal stress is measured counter-clockwise from the surface

91 normal of the dam.

2.3 Stress model

Thermal stresses in ice have been discussed in the context of elastic behavior over short periods of time, only (e.g. Comfort et al., 2003; Morse et al. 2011). However, ice is clearly not an elastic material and alternative formulations of ice rheology have been proposed (e.g., Royen, 1922; Lindgren, 1970; Drouin and Michel, 1974; Bergdahl, 1978). The model of Bergdahl (1978) enjoyed considerable success when compared with field measurements when the originally proposed coefficients were adjusted (e.g., Cox 1984; Fransson 1988). In addition, with only three parameters, this formulation is one of the simplest. Following Bergdahl (1987), the thermal stress in ice is described as a spring and non-linear dashpod model that can be expressed as

$$\frac{d\sigma}{dt} = E\left[\alpha\frac{dT}{dt} - KD\left(\frac{\sigma}{\sigma_0}\right)^n\right], \qquad (1)$$

where σ is the local stress (Pa), t is time (s), E the elastic modulus of ice (Pa), α the thermal expansion of ice (α=5x10^{-5} K^{-1}), T the ice temperature (°C), D the temperature-dependent viscous creep rate (m²/s), K (m^{-2}) and n coefficients of viscous deformation, and σ_0 an arbitrary reference stress for dimensional consistency (Pa). The temperature-dependent elastic modulus of ice is

$$E = E_0(1 - CT), \qquad (2)$$

where C=0.012 K^{-1} (Bergdahl, 1978). While Bergdahl (1978) used E_0=6.1 GPa, Cox (1984) suggested the use of E_0=4 GPa since strain rates are low (Traetteberg et al., 1975). Bergdahl's choice of the Arrhenius equation to describe the temperature-dependence of the creep rate was questioned by Cox (1984), arguing that this relationship does not hold at high temperatures. Instead, based on very limited data, Cox (1984) suggested replacing KD with an expression

$$KD = \beta\left(\frac{T_1}{T}\right)^m, \qquad (3)$$

113   where $T_1 = -1$ °C is a constant for dimensional scaling, and $\beta = 2.46 \times 10^{-29}$ s^{-1} and $m = 1.92$ are fitted

114   constants.

115   Fransson (1988) allowed all parameters to be fitted to data and, to avoid the singularity at 0 °C,

116   suggested

117      $$KD \propto \left(\frac{T_1}{T_1 + T} \right)^m . \qquad (4)$$

118   Following Bergdahl and Wernersson (1978), Cox (1984) chose $n = 3.7$.

119   In this study stress was modeled stress as

120      $$\frac{d\sigma}{dt} = A\frac{dT}{dt} - B \left(\frac{T_1}{T} \right)^m \left(\frac{\sigma}{\sigma_0} \right)^n , \qquad (5)$$

121   where A, B, and n are temperature-independent constants. Constants m and T_1 are as given by Cox

122   (1984). However, three alternative formulations will be discussed, i.e.,

123      $$\frac{d\sigma}{dt} = A\frac{dT}{dt} - B \left(\frac{T_1}{T_1 - T} \right)^m \left(\frac{\sigma}{\sigma_0} \right)^n , \quad (6)$$

124   based on (4),

125      $$\frac{d\sigma}{dt} = (1 - C\,T) \left[A\frac{dT}{dt} - B \left(\frac{T_1}{T} \right)^m \left(\frac{\sigma}{\sigma_0} \right)^n \right] , \quad (7)$$

126   accounting for the temperature dependence of the elastic modulus (2), and

127      $$\frac{d\sigma}{dt} = A\frac{dT}{dt} - B \left(\frac{\sigma}{\sigma_0} \right)^n , \qquad (8)$$

128   assuming temperature-independence of all physical properties.

129   While formulations (5) to (8) are defined for positive stresses, only, the formulation has been

130   extended to negative stresses presumably the same way Cox (1984) did. This approach assumes that

131   tensile stresses do not lead to crack formation or other irreversible deformation. Using (5) as an

132   example, the model was implemented as

133   $$\frac{d\sigma}{dt} = A\frac{dT}{dt} - \text{sign}(\sigma) B \left(\frac{T_1}{T}\right)^m \left(\frac{|\sigma|}{\sigma_0}\right)^n , \qquad (9)$$

134   where the sign(x) function evaluates to +1 for $x>0$, -1 for $x<0$ and 0 for $x=0$.

135   The model equations were solved using explicit time integration since ice temperature and stress

136   data were recorded at intervals as short as 5 minutes. Parameters A, B, and n were fitted by

137   minimizing the residual with a simplex algorithm (Nelder and Mead, 1965). In cases where the

138   optimal common parameters for a group of stress cells has been determined (e.g., a common A and n

139   for a group of cells while each cell differs in B), the sum of the residuals of the individual cells was

140   minimized.

141   We chose as reference case Equation (9) with A=200 kPa/°C and n=3.7 (following Cox (1984)) and B

142   fitted to measurements. Unless specified otherwise, parameters were fitted to measurements of the

143   combined period of 9 to 19 March and 26 March to 4 April as these were periods dominated by

144   compression and spanned a wide range of ice temperatures.

145   # 3   Results

146   ## 3.1   Ice conditions

147   As common for reservoirs, the ice cover grew as congelation ice, snow-ice and superimposed ice

148   from flooding (e.g., Carter et al., 1998; Stander, 2006; Morse et al., 2011; Leppäranta, 2015). At the

149   time of deployment, ice thickness near the dam and at the center of reservoir was 0.75 m and 1.2 m,

150   respectively, with 0.2 to 0.32 m snow depth at all stations except Station 5. Winds sweeping from the

151   east had reduced snow depth to 0.05 m at Station 5.

152   Temperature data showed that the water was stratified until a warm spell occurred at the end of

153   February (Petrich et al., 2014). Throughout March and April water was mixed presumably due to a

154   steady flow of water moving through the reservoir. This flow across the spillway prevented water

155   level fluctuations and the build-up of pressure in the reservoir (Petrich et al., 2014).

156   Ice conditions in Season 2012/13 were nearly ideal for the measurement of thermally-induced

157   stresses. For convenience of the discussion, the measurement period discussed here was divided into

158   several phases (Table 2). When stress cells froze into the ice cover in mid-February high initial

159   stresses were recorded (reaching up to 1 MPa) due to volume expansion during freezing of

160   surrounding water (e.g. Cox, 1984; Carter et al., 1998). Stress readings returned to their original zero-

161   reading during a warm spell from 24 February until 1 March in all near-surface cells (i.e., 1, 2, 3-top,

162   4, 5-top, 6, W-top, N, and S). During the subsequent temperature decrease (phase 1a), none of those

163   cells showed freeze-in artifacts of magnitude or duration observed in mid- February. This resulted in

164   approximately six weeks of quality data of thermal stresses until the ice finally decayed starting 14

165   April (phase 6). The warm spell in February resulted in approximately 0.05 m ice ablation at the

166   surface, i.e. the centers of the cells discussed here were at a depth of 0.15 m in the ice.

167   Episodes of snowfall ensured that the ice was continuously snow-covered from 4 Mar until 16/17

168   April with snow depth 0.1 m or more at the measurement stations (Figure 4). The exception was

169   phase 3 which started with wind reducing the snow cover to as little as 0.05 m at Station 5 on 19

170   March. Hence, radiative heating of the ice and cells was not of major concern. There was a small (3

171   m^2), localized flooding event confined a patch of ice between Stations 5 and 6 on 8 March (followed

172   by snowfall on 9 March, phase 2a), and a more extended event near the NW and SW corners of the

173   reservoir (approx. 100 m^2 each) on 20 March (followed by snowfall on 22 March, phase 3). These

174   locations were observed to experience flooding during cold spells throughout the winter (i.e., also

175   before February) and coincided with the locations of a known crack (cf. Stander, 2006). Neither

176   flooding reached a measurement station.

3.2   Temperature registered by stress cells

178   Figure 5 shows temperatures registered by the stress cells. Temperatures registered by stress cells 2,

179   3-top, 5-top, and 6 were very similar to each other (spread <0.2 °C) while temperatures at cells W-

180   top, N, and S were systematically lower (up to 0.5 °C). Temperatures at cells 1 and 4 were higher and

181   showed less variability than any of the other cells, resulting from deeper snow cover locally. Based on

182   these observations, a temperature representative of the near-surface conditions of the ice sheet was

183   calculated as arithmetic mean of cells 2, 3-top, 6, W-top, N, and S. Temperatures of cell 5-top were

184   not used because the temperature signal was noisy, presumably due to a bad electrical contact. The

185   representative temperature was used for ice stress modeling.

186   After an initial drop of the representative ice temperature to -9 °C in phase 1a in response to a

187   decrease in air temperature, ice temperatures increased with periodic oscillations until the beginning

188   of phase 5 with the exception of a cold spell in phase 3 (-8 °C). The low ice temperatures in phase 3

189   were due to winds reducing the depth of the snow cover and increasing turbulent heat transfer.

190   Diurnal temperature variations became evident in March in phase 4a, and persistent ice

191   temperatures above –1 °C were observed in phase 4b. Ice temperatures stayed between -2 and -1 °C

192   throughout phase 5. Phase 6 marks the onset of ice decay with ice temperature increasing to the

193   melting point.

3.3   Normal stresses close to the dam

195   Stresses measured along the dam spanned the range from –100 kPa (tension) to +200 kPa

196   (compression). The ability of sensors to register tension was limited by a combination of cracks

197   opening in the ice over, finite adhesion of the sensor to the ice, and theoretically expected boiling of

198   the oil inside the cells at pressures below –100 kPa. Tension has been observed during phases 1a, 3,

199   and 5b (Figure 6), each of which coincided with decreasing ice temperatures (Figure 5).

200   Figure 7 shows examples of horizontal profiles of normal stresses recorded by the surface-most cells

201   in front of the dam. Prior to the end of March, highest stresses were observed at the center of the

202   dam. Around the turn from March to April, stresses were highest south of the center, while ice at the

203   center tended to be in tension in early April. There were periods with relatively evenly distributed

204   stresses (e.g. 1 April) and periods with distinct localized stress maxima (e.g. 25 March).

205   Time series of individual sensors are shown in Figure 6. Initial cooling took place during phase 1a,

206   followed by another brief cold spell in phase 1b. Compressive stress oscillated with a period of 4

207   stress maxima over the course of 14 days in phase 2. A cold spell in the ice had been experienced

208   during phase 3. The ice warmed up continuously during phase 4 with a small superimposed diurnal

209   temperature and stress signal. Stress magnitudes were small during phase 5, showing both tension

210   and compression. Ice temperatures increased to the melting point in phase 6. The highest stresses

211   were recorded at the end of the cold spells, i.e. in phase 1b and at the end of phase 3.

212   Using A and n as in Cox (1984), parameter B of the model of Equation (9) was fitted to the data. The

213   model was driven with the representative ice temperature for the depth of the cell rather than the

214   locally observed stress cell temperature. The difference is illustrated in Figure 9 which shows that the

215   stresses measured during phase 4a were much better correlated with the representative ice

216   temperature than with the local stress cell temperature. This difference most likely resulted from a

217   thermally insulating snow drift in front of the maintenance hut, extending to Station 4.

218   Figure 6 compares model predictions with measured stresses. In spite of its simplicity, and although

219   only phases 2b, 4a since 26 March, and 4b were used for fitting, the model results agree very well

220   with observations throughout the season.

221   The fitted factor *B* shows systematic behavior, decreasing from the flanks of the reservoir (Stations 1

222   and 6, *B*=24000 kPa/day) toward the center (Station 4, *B*=340 kPa/day) (Figure 8). *B* appears to

223   change by a factor of approximately 10 over the course of 10 m. We are not aware of other reports

224   of a systematic, spatial variation of coefficients in a reservoir. Our fitted values *B* are large compared

225   to those of Cox (1984), who used *B*=27 kPa/day in a setting that was laterally essentially

226   unconstraint. Hence, in addition to creep (which is spatially independent), *B* also includes (spatially

227   dependent) effects due to spatially varying boundary conditions, crack pattern, and possibly ice

228   thickness and texture.

3.4 Principal stresses

230   The principal stress direction varied systematically (by approximately 90°) at the beginning and end

231   of each cold spell lasting for about five days. Figure 10 shows the principal stresses and the stress

232   data of cells N, S, and W-top they were derived from. Periods of temperature increase (phases 2, 4,

233   5b, and 6) were associated with a counter-clockwise rotation of the principal stresses. Cold spells

234   (phases 1a, 3, 5a, and 5c) started with a clockwise rotation of typically 90° that aligned the first

235   principal stress in NW–SE direction. It is interesting to note that the first principle stress is generally

236   aligned parallel to the dam. This appears to be consistent with other observations (e.g., Cox, 1984;

237   Morse et al., 2011). Morse et al. (2011) attributed this to the presence of cracks parallel to the dam

238   that harbor the potential to relieve stress. However, in the present case it could be related to the

239   boundary conditions of the reservoir.

4 Discussion

241   While the model does an excellent job reproducing the stress history of the reservoir, in particular

242   during times of compression, it still relies on a single, location-dependent parameter that, so far,

243   needs to be fitted to data. However, of most concern to design are maximum loads. In some cases

244   the model predicted peak magnitudes that were not observed in cells. If one assumes that this is due

245 to natural inhomogeneity of the ice then otherwise accurate models may need to include calibration

246 factors to down-correct average loads on dams. Another possibility that should be considered is that

247 measurements are at error, for example due to local changes in ice properties during the freeze-in

248 period of the cell.

249 ## *4.1 Normal stresses*

250 The model of Bergdahl (1978) has been shown to be successful for stresses normal to a dam or

251 shore. Ice stresses were investigated in one of the smallest reservoirs ever reported, and a

252 systematic dependence of one parameter on location was found. It is obvious that the model in its

253 current form cannot describe the biaxial stress field without additional considerations (e.g., Fransson,

254 1988). At the same time, this failure is reassuring us that the stresses measured were indeed brought

255 about by the entire ice sheet rather than generated locally at the stress cells. However, it also serves

256 as a reminder that Equation (5) is first and foremost an empirical model, and that its applicability

257 appears to be limited to stresses normal to and close to a rigid boundary.

258 A striking observation of the fitted parameters of Equation (5) is that parameter B depends

259 systematically on the position of the cell. It was lowest at the center of the dam where the sensitivity

260 of load to temperature changes was highest and decreased toward either end of the dam (Figure 8).

261 Based on the introduction of Equation (5) one would have expected B to be an intrinsic material

262 property of ice only. However, B depends obviously on measurement location with respect to the

263 boundary configuration. In addition, B may depend on the crack pattern and possibly systematic

264 variations in ice thickness and texture. Both would result from the reservoir shape (cracks as a result

265 of stresses, and thickness variations as a result of flooding through cracks), making it impossible to

266 determine the physical origin from the current data set. A general procedure to determine the

267 apparent parameters A, B, and n (e.g., from rigorous numerical modeling) would greatly facilitate

268 stress calculations.

4.2 Model parameters

We noticed that it is possible to obtain reasonable fits using the same parameters *A* and *n* for all cells, only determining *B* individually for each cell. In contrast, it is not possible to do the same with common *B* and *n*, varying *A*. A lot of time can be spent on finding optimal parameters as the best fit depends somewhat on the time interval used for fitting. In the current case, the mathematically most optimal values for *A* and *n* common to all cells were determined to be *A*=179 kPa/°C and *n*=4.5. Forcing *n*=3.7 and *n*=3, the optimal value would be *A*=156 kPa/°C and *A*=131 kPa/°C, respectively. While the combination 179/4.5 presents a slight improvement of the fit, the combination 131/3 still results in a reasonable fit with the possible exception of phases 1a and 1b where stresses are underpredicted significantly for cells 3-top and 4 (not shown). One may argue that the amount of insight is limited that can be gained from curve fitting alone, and we do not recommend an optimal set of parameters. Values in the range of *n*=1 to *n*=4 have been reported (e.g., Drouin and Michel, 1974; Song et al., 2006; Duval et al., 2010). However, one can gain insight from an analysis of temperature dependence of the assumed physical properties.

The performance of model equations (5) to (8) will be compared next to identify the best compromise between number of parameters and quality of fit to observations. Using model equations (6) to (8), the following observations were made (not shown): fitted results based on (6) are very similar to those of (5). The peaks in phases 1b and 2a of cells 3-top, 4, and 5-top are better predicted by (6) while the discrepancy in phase 4b of cells 3-top and 4 is larger. The latter is of particular concern as it appears to indicate that the increase of the creep rate with temperature is underestimated by (6) (note that this assessment assumes that *n*=3.7 is a valid assumption for both equations). Using (7) instead of (5) further exaggerates the modeled peaks in phases 1b, 2a and at the transition from phase 3 to 4a of cells 3-top, and 4 (not shown). Hence, we have no evidence that accounting for a temperature dependence of the elastic modulus leads to practical improvements of the model. It appears that more data both at low ice temperatures (i.e., <-10 °C) and close to the

294   melting point of ice (i.e., >-1 °C) would be required to assess this further. Using temperature-

295   independent ice properties in (8), some features are fitted slightly better while other features are

296   fitted slightly worse than with (5) (Figure 9c). The fit to cell 2 improves in every phase (not shown).

297   However, the most striking discrepancy appears in phase 4b with stresses systematically

298   overpredicted for cells 3-top, 4, and 5-top (Figure 9c). Phase 4b was marked by ice temperatures

299   above -1 °C, suggesting that creep rate increase with temperature is an important feature for the

300   range of ice temperatures observed in this study. While this conclusion is not new, there seem to be

301   few examples of this effect in the literature. We conclude that equation (5) captures the most

302   significant processes required to reproduce thermal loads of our measurement: elasticity and

303   thermal expansion of the ice cover, creep relaxation, and temperature-dependence of the creep rate.

304   However, in the light of spatial variability of B, other effects could need to be included.

4.3 Principal stresses

306   A simple numerical model of the stress field was used to verify the hypothesis that the rotation of

307   the principal stresses is real and could have been caused by uneven ice temperature change without

308   the need to invoke cracks. Although ice experiences creep, a simple thermoelastic model was used to

309   study potential stress distribution qualitatively. Using the TNO DIANA™ software package, numerical

310   simulations were performed of a square, thermoelastic plate of size 30 m x 30 m (α=5x10^{-5} K^{-1},

311   E=5 GPa) with boundaries fixed at three sides, representing a simplification of Taraldsvikfossen

312   Reservoir (Figure 11). By design, the material was stress-free at -3 °C. The initial temperature of the

313   material was 0 °C, i.e. the material experienced compressive stress throughout the entire domain.

314   The stress field was calculated while the temperature of the upper-left hand side quadrant was

315   reduced to –4 °C. The development of the stress field is shown in Figure 11. Initially, the material was

316   under compressive stress and the first principal stress at the marked location was aligned

317   approximately parallel to the direction of confinement (Figure 11a). As the material warmed in the

318   upper left hand side quadrant (Figure 11b, temperature in the quadrant was –2.3 °C), reducing the

319 stresses, the direction of the principal stress changed clockwise at the location marked below.

320 Eventually, the material in the upper left hand side quadrant experienced tensile stress (Figure 11c,

321 temperature –4 °C), imposing essentially no compressive forces on the remaining material in the

322 domain. The whole process resulted in a rotation of the principal stresses by approximately 90° in the

323 quadrant below (e.g. point circled in Figure 11a to c). The direction of the first principal stress circled

324 in Figure 11 is shown in Figure 12 as a function of temperature in the upper left and side quadrant,

325 illustrating that the transition was continuous but non-linear.

326 The simple numerical model cannot describe the stress field in the ice cover of Taraldsvikfossen

327 Reservoir accurately. For example, the shape of the domain and boundary conditions are not

328 accurate, both temperature distribution and temperature evolution are oversimplified, material

329 properties are not temperature-dependent, creep of the material is ignored and cracks are not taken

330 into account. However, it illustrates that a significant rotation of the principal stresses may well be

331 due to differential temperature development in the ice and would be related to measurement

332 position with respect to the boundary. Hence, biaxial measurements in conjunction with a numerical

333 model could help specify the boundary conditions of a small reservoir.

5 Conclusions

335 In this study, spatially distributed ice stresses were measured in a small reservoir over the course of

336 several weeks and the simple model of Bergdahl (1978) was used to describe thermal stresses in the

337 ice cover of a small reservoir. The agreement between model and observations was surprisingly

338 good. The measurements showed that an uneven snow cover led to a spatially and temporally

339 varying stress field. Comparing measurements and model, evidence of opening and closing cracks

340 was found. The cracks did not seem to adversely affect the ability to model stresses normal to the

341 boundary except that the magnitude of stresses in tension was overpredicted.

342 It was found that the temperature dependence of the creep rate is an important aspect to consider if

343 ice temperatures range from -9 °C to temperatures close to the melting point. The approach of Cox

344 (1984) worked well in this study even though it was based on a small set of data. There is potential

345 for further improvement based on better knowledge of temperature-dependent ice properties.

346 One parameter used in the Bergdahl (1978) ice load model was found to vary systematically with

347 location (i.e., parameter B) with the lowest value observed at the center of the dam. This implies that

348 actual ice rheology can be difficult to determine from measurements in small reservoirs. Since the

349 stress field should be homogeneous in a completely confined ice sheet, the spatial dependence of

350 stresses registered in the ice and the systematic rotation of the principal stresses both point toward

351 the absence of confinement at some section of the boundary. However, the systematic dependence

352 of model parameters on location suggests that it should be possible to model spatial and temporal

353 variability of stresses in small reservoirs numerically. In particular, earlier work found encouraging

354 agreement between numerical models and field and laboratory measurements (Azarnejad and

355 Hrudey, 1998). Numerical models using intrinsic material properties and appropriate boundary

356 conditions may be used to estimate effective parameters of models such as Equation (5). In this

357 context one may also wish to consider the structure's ability to deform (CFBR, 2013). In order to gain

358 experience in defining numerical boundary conditions, biaxial measurements should be performed in

359 reservoirs. A better understanding of the stress distribution will help in experiment design. With

360 computational resources available today, a better understanding of thermal ice loads is within reach.

361 However, more data on small reservoirs without waterlevel fluctuations may be needed.

Acknowledgements

References

Azarnejad, A., and T. M. Hrudey (1998). A numerical study of thermal ice loads on structures, Canadian Journal of Civil Engineering, 25(3), 557-568. http://dx.doi.org/10.1139/l97-119.

Bergdahl, L. (1978). Thermal ice pressure in lake ice covers. Report Series A:2, Department of Hydraulics, Chalmers University of Technology, Göteborg, Sweden, 164 pp.

Bergdahl, L., and L. Wernersson (1978). Calculated and expected thermal ice pressures in five Swedish lakes. Chalmers University of Technology, Göteborg, Sweden, Report Series B:7. 82pp.

Carter, D., D. Sodhi, E. Stander, O. Caron, and T. Quach (1998). Ice thrust in reservoirs. Journal of Cold Regions Engineering, 12(4), 169–183. http://dx.doi.org/10.1061/(ASCE)0887-381X(1998)12:4(169).

CFBR (2013). Guidelines for the justification of the stability of gravity dams. French Dams and Reservoirs Committee (CFBR), Le Bourget-du-Lac, France. 92pp.

Comfort, G., Y. Gong, S. Singh, and R. Abdelnour (2003). Static ice loads on dams. Canadian Journal of Civil Engineering, 30, 42–68. http://dx.doi.org/10.1139/L02-080.

Cox, G. F. N. (1984). A preliminary investigation of thermal ice pressures. Cold Regions Science and Technology, 9. 221–229.

Cox, G. F. N. and J. B. Johnson (1983). Stress measurements in ice. Report 83-82, Cold Regions Research and Engineering Laboratories, Hanover, NH, USA. 31pp.

Drouin, M., and B. Michel (1974). Pressures of Thermal Origin Exerted by Ice Sheets upon Hydraulic Structures. Draft Translation 427. Cold Regions Research and Engineering Lab, Hanover, NH, USA. 429pp.

Duval, P., M. Montagnat, F. Grennerat, J. Weiss, J. Meyssonnier, A. Philipp (2010). Creep and plasticity of glacier ice: a material science perspective. Journal of Glaciology, 56(200), 1059–1068.

392   Fransson, L. (1988). Thermal ice pressure on structures in ice covers. Ph.D. Thesis, Luleå University of

393   Technology, Luleå, Sweden, 161 pp.

394   Gebre, S., Alfredsen, K., Lia, L., Stickler, M., and E. Tesaker (2013). Review of ice effects on

395   hydropower systems. Journal of Cold Regions Engineering, 27(4), 196–222.

396   Holister, G. S. (1967). Experimental Stress Analysis. Cambridge Engineering Series, Cambridge

397   University Press, Bentley House, London, UK, 321pp.

398   Hoseth, K. A., and L. Fransson (1999). Istrykk på dammer, Måleprogram dam Silvann, vinter 98-99.

399   Norwegian Water Resources and Energy Directorate (NVE), Oslo. Report 22/1999. 34pp.

400   Leppäranta, M. (2015). Freezing of Lakes and the Evolution of their Ice Cover. Springer, New York,

401   301 pp.

402   Lindgren, S. (1970). Thermal ice pressure. In Proceedings of the IAHR Symposium on Ice and its

403   Actions on Hydraulic Structures. Reykjavik, Island. 6.7.1–6.7.40.

404   Ministry of Petroleum and Energy (2009). Forskrift om sikkerhet ved vassdragsanlegg

405   (damsikkerhetsforskriften). FOR-2009-12-18-1600, Ministry of Petroleum and Energy, Oslo, Norway.

406   Morse, B., E. Stander, A. Côté, M. Richard, and V. Desmet (2011). Stress and Strain dynamics in a

407   hydro-electric reservoir ice sheet. In Proceedings of the 16th Workshop on the Hydraulics of Ice

408   Covered Rivers, Winnipeg, MB, Canada, 18–22 September 2011, 303–316.

409   Nelder, J. A., and R. Mead (1965). A Simplex Method for Function Minimization. The Computer

410   Journal, 7, 308–313.

411   NVE (2003). Retningslinje for laster og dimensjonering til §§ 4-1 og 4-2 i forskrift om sikkerhet og

412   tilsyn med vassdragsanlegg Norges vassdrags- og energidirektorat. Norwegian Water Resources and

413   Energy Directorate (NVE), Oslo, Norway. 25pp.

414   Petrich, C., I. Sæther, L. Fransson, B. Sand, and B. Arntsen (2014). Preliminary results from two years

415   of ice stress measurements in a small reservoir, In Proceedings of the 22nd IAHR International

416   Symposium on Ice, Singapore. 452-459.

417   Royen, N. (1922). Ice pressure with increasing temperatures. Draft Translation 45 (1955). Cold

418   Regions Research and Engineering Laboratory, Hanover, NH, USA.

419   Stander, E. (2006). Ice stresses in reservoirs: effect of water level fluctuations. Journal of Cold

420   Regions Engineering, 20(2), 52-67.

421   Song, M., D. M. Cole, and I. Baker (2006). Investigation of Newtonian creep in polycrystalline ice.

422   Philosophical Magazine Letters, 88(12), 763–771.

423   Taras, A., A. Côté, G. Comfort, L. Thériault, and B. Morse (2011). Measurements of ice thrust at

424   Arnprior and Barrett Chute dams. In Proceedings of the 16th Workshop on the Hydraulics of Ice

425   Covered Rivers, Winnipeg, MB, Canada, 18–22 September 2011, 317–328.

426   Traetteberg, A., L. W. Gold, and R. Frederking (1975). The strain-rate and temperature dependence

427   of Young's modulus of ice. In Proceedings of the Third IAHR International Symposium on Ice

428   Problems, Hanover, NH, USA. 479–486.

429   Timco, G.W., D. A. Watson, G. A. Comfort, and R. Abdelnour (1996). A comparison of methods for

430   predicting thermally-induced ice loads. Proceedings of the 13th IAHR Symposium on Ice, Beijing,

431   China, vol. 1, 241-248.

432

Tables

433 **Tables**

434 Table 1. Position of stress cells. Lateral position is measured from the center of dam, except Stations

435 1 and 6 which are measured from the respective corners of the dam. Negative numbers are to the

436 South. Normal position is measured perpendicular to the dam face.

Station	1	2	3	4	5	6	N	S	W
# of cells	1	3	1	3	3	1	1	1	3
Lateral (m)	-4.2	-10.3	-5.9	-0.3	9.4	6.4	0.7	0.7	0.7
Normal (m)	1.2	1.1	1.1	1.1	1.4	1.8	7.8	7.8	7.8

437

438

439

440   Table 2. Division of the measurement period into phases based on stresses at cells 1, 2, 3-top, 4, 5-

441   top, and 6: general stress state (compression/tension), distribution (evenly/uneven with pronounced

442   peak), location of peak stress with respect to center of the dam (North or South), and general near-

443   surface ice temperature.

Phase	Date	State	Distribution	Peak stress	Ice temp
-	until 1 March (noon)	no stress			high
1a	1 to 5 March (am)	tension	uneven	N	
1b	5 to 7 March (am)	compression			
2a	7 to 9 March (am)	compression	even	S	
2b	9 to 19 March (pm)	compression	even	S	
3	19 to 23 March (midnight)	tension	uneven	N	
4a	23 to 31 March (pm)	compression	even	S	
4b	31 March to 5 April (am)	compression	even	S	high
5a	5 April to 8 April (noon)	tension	uneven	N	
5b	8 April to 12 April (am)	stresses around 0			
5c	12 April to 14 April (pm)	tension	uneven	N	
6	14 April to 17 April (am)	compression	even	S	high
-	from 17 April	no stress			high

444

445
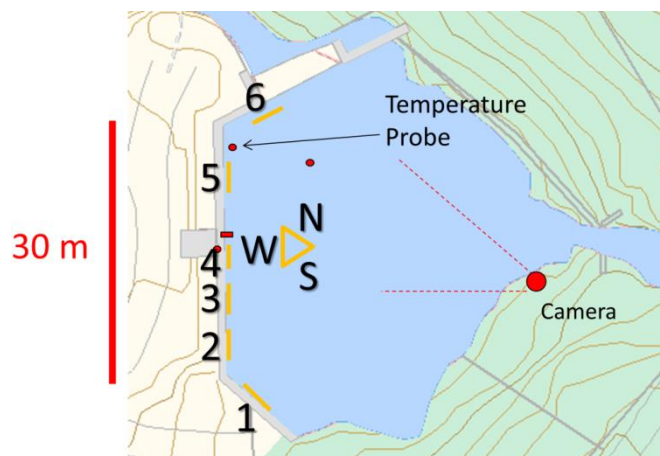
Figures

448   Figure 1. Sketch of the approximate locations of the load cells deployed on 12 February 2013.

449   Markers indicate station name. North is up. Map source: NVE Atlas.

450

451
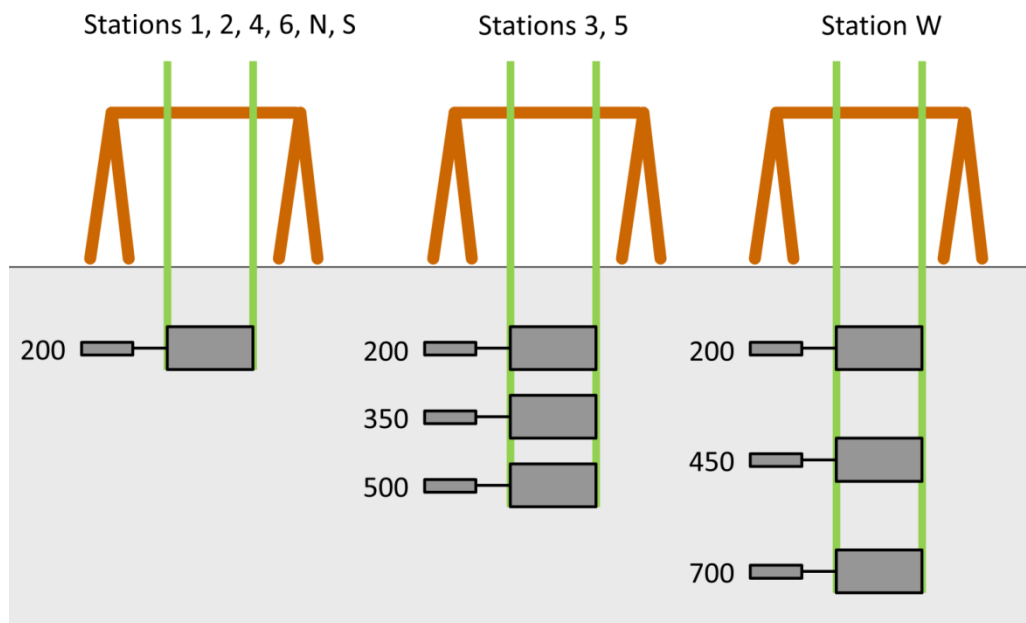
453   Figure 2. Configuration of pressure cells (large rectangles) at 9 measurement stations. Depths of the

454   centers of the vertical cells are given in mm below ice surface at the time of deployment.

455
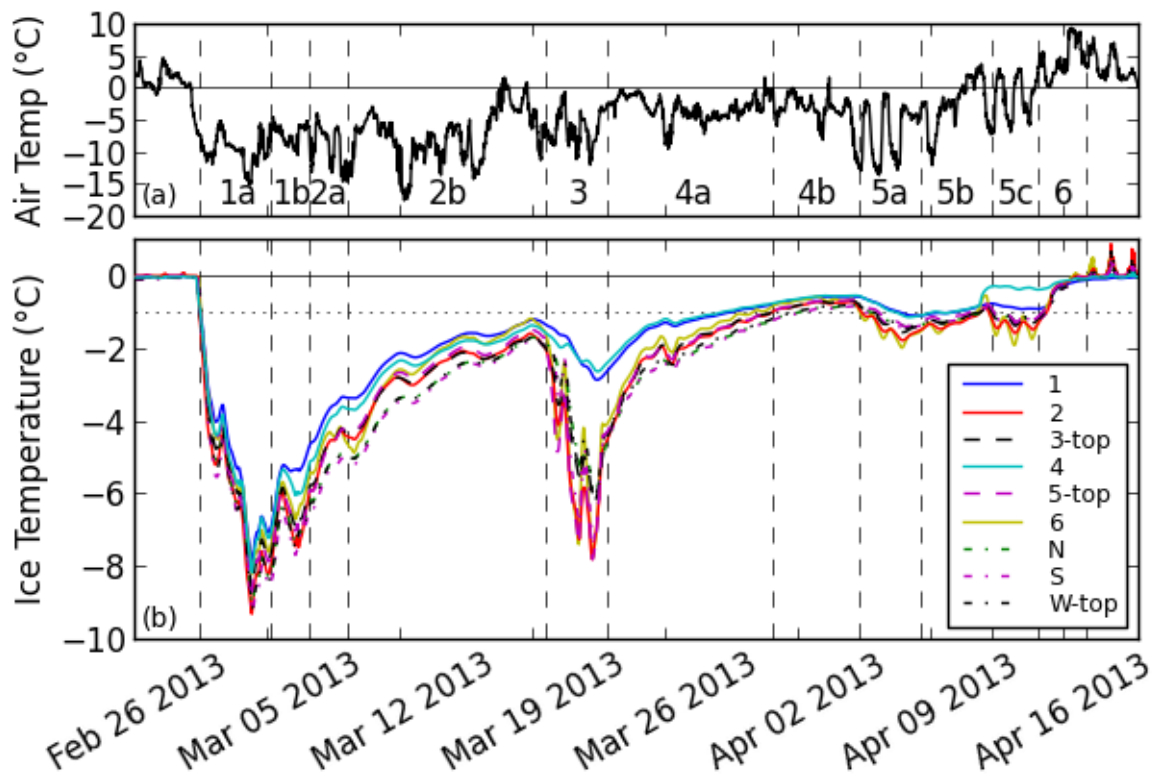
456

457

458   Figure3. Installation of stress cells at Station 5 on 12 February 2013.

459

460

461

462   Figure 4. Overview of snow-covered site on 23 March 2013. View is toward North.

463

464

465

Figure 5. (a) Air temperature and (b) temperatures registered at the top-most cell of each station.

The dotted line at −1 °C is for visual reference to particularly warm ice.

468
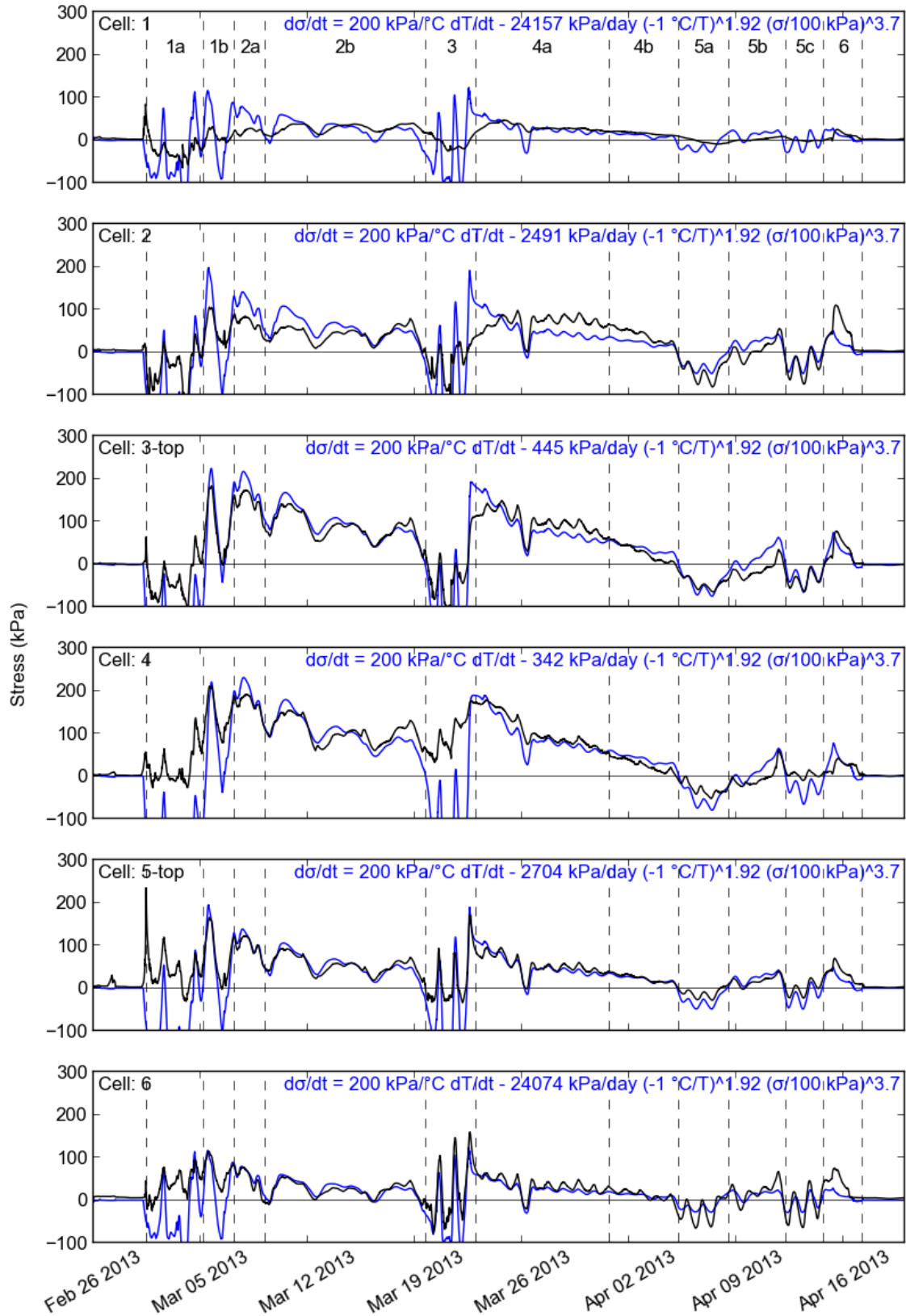
469

470 Figure 6. Stresses registered in the near-surface cells along the dam (black lines). All simulations use

471 average temperature registered at stations with thin snow cover (blue lines).

472
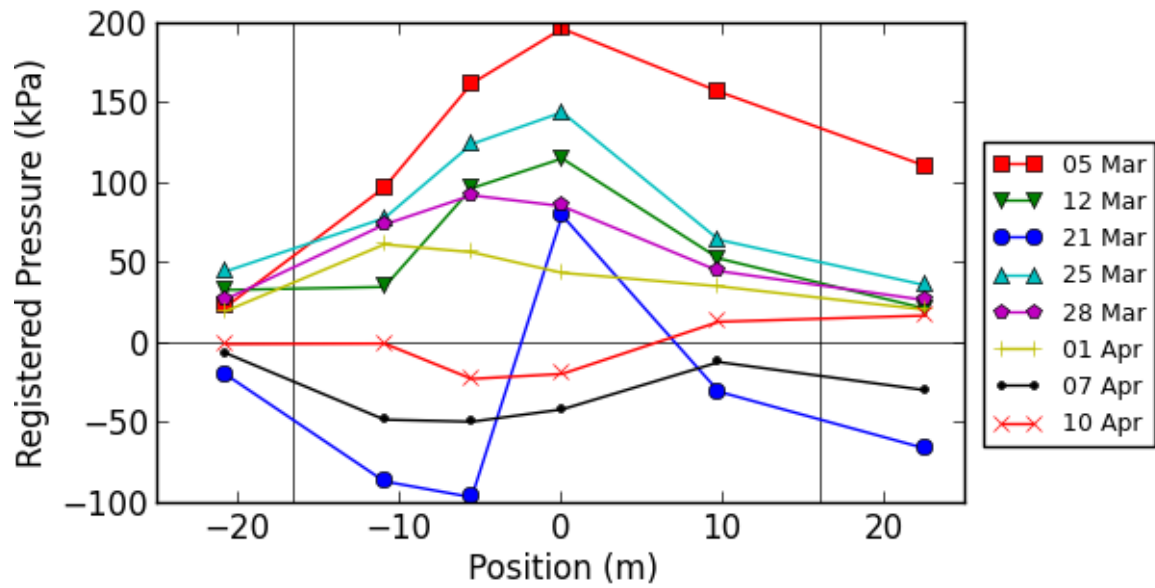
Figure 7. Examples of pressure distribution at the top-most cells of stations 1 to 6. Data of midnight

UTC, except 12:00 on 5 Mar 2013. The vertical lines mark the limits of the main section of the dam

(i.e., S–N section). The *x*-axis shows linear distance from the center of the dam with negative values
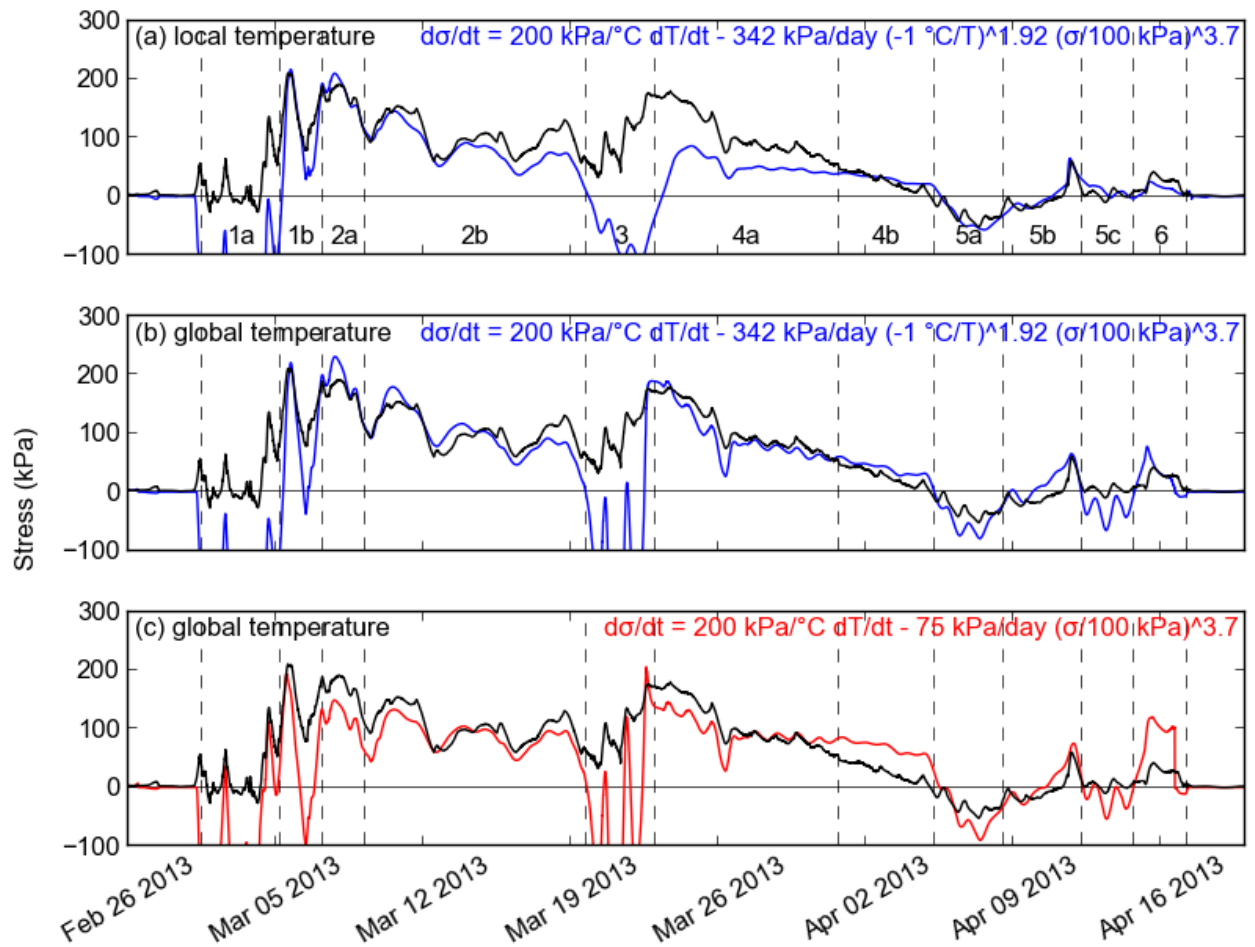
South (i.e., Stations 1 to 3).

477
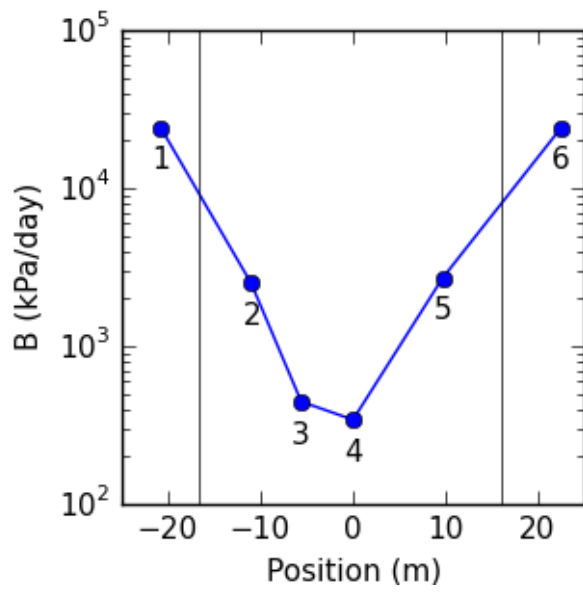
478

479   Figure 8. Distribution of fitted parameter *B* (Figure 6) along the stations (labels). The vertical lines

480   mark the limits of the main section of the dam (i.e., S–N section). The *x*-axis shows linear distance

481   from the center of the dam with negative values South (i.e., Stations 1 to 3).

482

483   Figure 9. Comparison of data from cell 4 data (black line) modeled with (a) temperature measured at

484   cell 4, and (b) representative ice temperature characteristic for the ice sheet at large, and (c) with

485   representative ice temperature and temperature-independent creep.

486

487
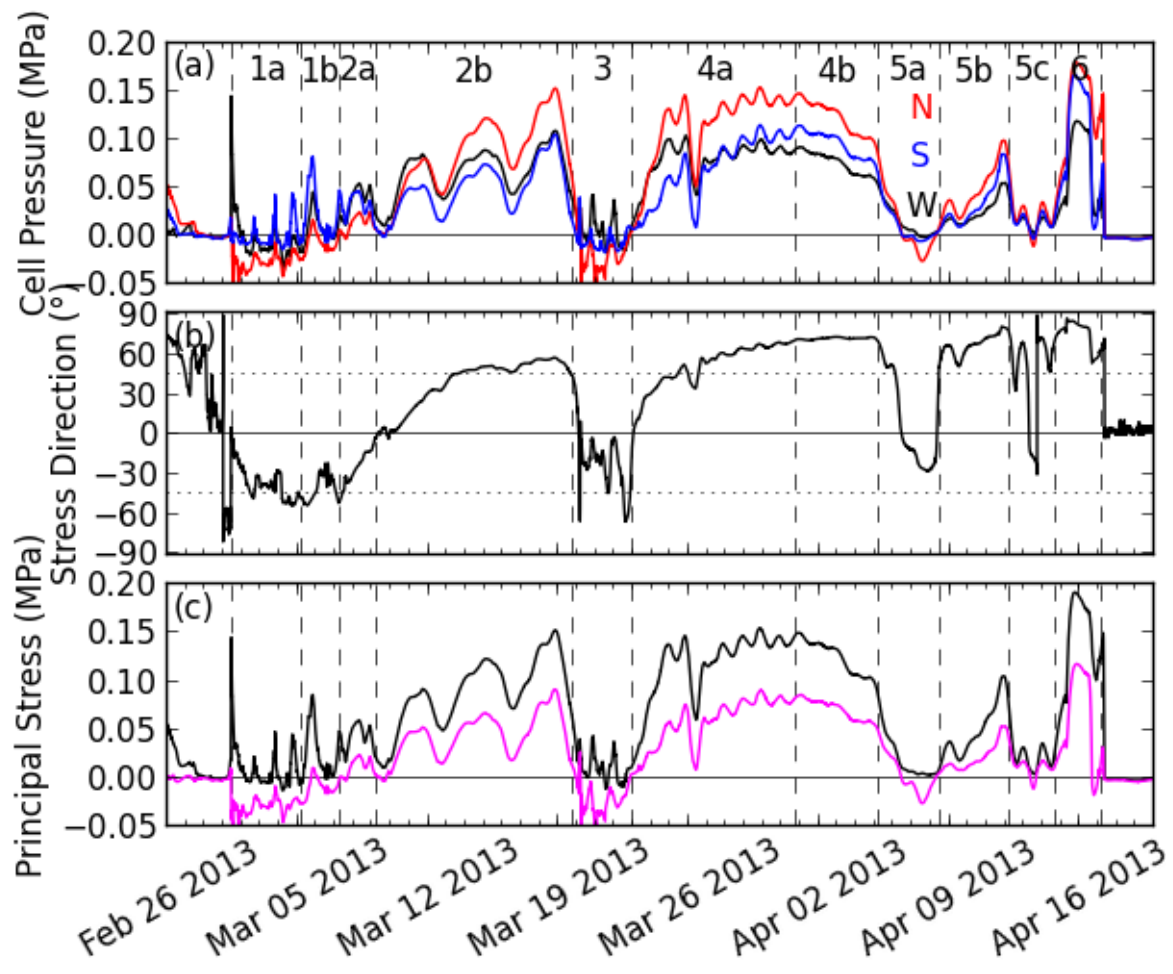
Figure 10. Principal stresses derived from cells N, S, and W-top. (a) Data of cells N (red), S (blue), and

W-top (black), (b) Direction of the first principal stress, (c) magnitude of first (black line) and second

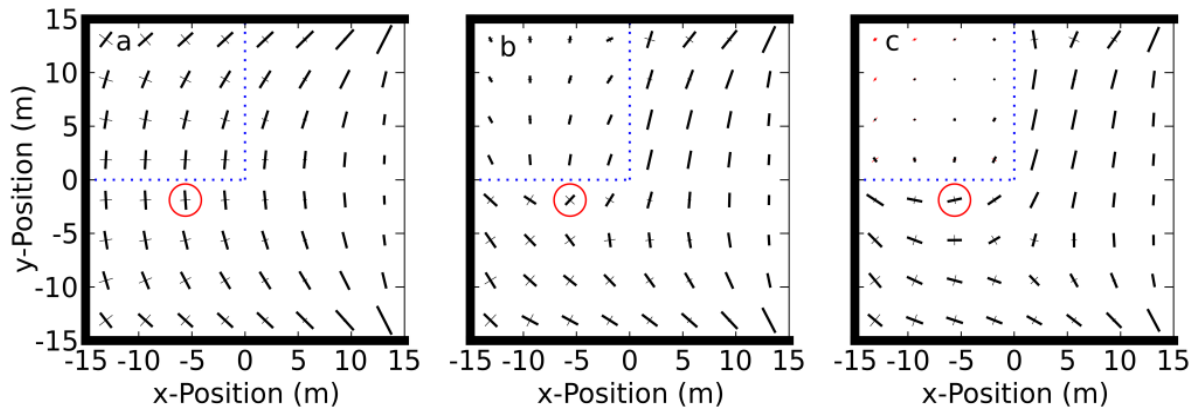(purple line) principal stresses.

Figure 11. Direction of the principal stresses in a thermoelastic materials confined at the upper, left, and lower boundary (first principal stress: thick lines, second principal stress: thin lines). Length of stress lines is proportional to stress magnitude. The angle of the principle stress at the point circled is shown in Figure 12. (a) Homogeneous temperature throughout the domain, resulting in compressive stresses; (b) reduced temperature in upper left hand side quadrant (separated by dotted line), resulting in lower stress magnitudes and rotation of principal stress directions; (c) further reduced temperature in upper left hand side quadrant, resulting in tension (short red lines in upper left hand corner) and further rotation of principal stress directions.

501
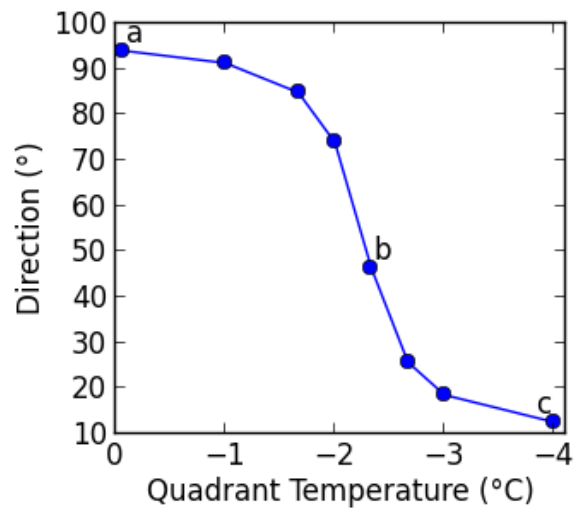
502 Figure 12. Direction of the first principal stress (thick lines in Figure 11) versus temperature of upper

503 left hand side quadrant of the domain. The temperature of the remaining domain is 0 °C. Data shown

504 are of point $x=-5.6$ m, $y=-1.9$ m in Figure 11, markers a to c correspond to subplots of Figure 11.